

M. LISOWSKI<sup>✉</sup>  
P.A. LOUKAKOS  
U. BOVENSIEPEN  
J. STÄHLER  
C. GAHL  
M. WOLF

# Ultra-fast dynamics of electron thermalization, cooling and transport effects in Ru(001)

Fachbereich Physik, Freie Universität Berlin, Arnimallee 14, 14195 Berlin, Germany

Received: 12 June 2003/Accepted: 4 July 2003

Published online: 31 October 2003 • © Springer-Verlag 2003

**ABSTRACT** Time-resolved two-photon photoelectron spectroscopy is used to study the dynamics of non-equilibrium electron and hole distributions at bare and D<sub>2</sub>O-covered Ru(001) following optical excitation (55-fs, 800-nm pulses) with variable fluence (0.04–0.6 mJ cm<sup>-2</sup>). Within the first 0.5 ps we observe an ultra-fast transient of the excited-carrier population and energy density at the surface which is accompanied by pronounced deviations of the electron-energy distribution from a (thermalized) Fermi–Dirac distribution. Comparison of the transient energy density of the photoexcited electrons at the surface with predictions of the two-temperature model provides fair agreement up to 400 fs, but exhibits a systematically lower energy density at later times, where electrons and phonons are equilibrated. We propose that this reduced energy density at the surface originates from ultra-fast energy transport of non-thermal electrons into the bulk in competition to electron–phonon coupling at the surface. This is corroborated by extending the two-temperature model to account for non-thermal, photoexcited electrons, whereby quantitative agreement with experiment can only be achieved if ballistic transport and reduced electron–phonon coupling is incorporated for non-thermal electrons. Implications for surface femtochemistry are discussed.

**PACS** 78.47.+p; 71.38.-k; 73.40.-c

## 1 Introduction

The ultra-fast dynamics of elementary scattering processes in solids are key for a microscopic understanding of fundamental solid-state properties like electric conductivity or light–matter interaction. For example, scattering between electrons and phonons or impurities/defects on the femtosecond time scale was implicit already in the first microscopic theories of electrical resistance [1] and has been studied extensively under quasi-equilibrium conditions (e.g. in transport measurements) [2]. However, only the rapid advances of time-resolved laser spectroscopy during the past decades have allowed us to disentangle directly the different elementary scattering mechanisms of photoexcited carriers in, so far,

unprecedented detail [3]. In these experiments, an ultra-short light pulse induces an electronic polarization in the material. Quasi-elastic scattering leads to rapid dephasing and hence absorption of light, resulting in a non-equilibrium distribution of electron–hole pairs. This non-thermal carrier distribution will (i) redistribute its energy by scattering among the quasi-particles themselves via electron–electron (e–e) collisions, leading to internal thermalization of the electronic system and (ii) transfer energy to the lattice via electron–phonon (e–ph) scattering, leading to cooling and equilibration with the lattice. Depending on the material system and the optical excitation density, both processes (thermalization and cooling) may occur on similar or separate time scales. In bulk samples, the finite optical penetration depth will inevitably lead to a spatially inhomogeneous excitation. Therefore, ballistic and diffusive transport may strongly affect the observed energy relaxation dynamics near the surface. Such transport effects will be absent in homogeneously excited systems, like thin films, heterostructures or nanoparticles on insulating substrates.

In metallic systems, the dynamics of photoexcited electrons are governed by the high density of valence electrons, which leads to screening of the Coulomb interaction of quasi-particles with their surroundings, but also contributes to the available phase space for e–e scattering [4]. At low excitation densities ( $< 10^{-4}$  e<sup>-</sup>/atom), where photoexcited electrons interact predominantly with the (‘cold’) equilibrium part of the electron distribution, scattering rates can be described within the framework of Fermi-liquid theory, whereby different degrees of sophistication have been used to account for screening [4, 5]. A detailed discussion of this regime is beyond the scope of this paper and can be found elsewhere [6]. At high excitation densities ( $> 10^{-3}$  e<sup>-</sup>/atom), rapid thermalization via multiple collisions among the photoexcited non-equilibrium electrons (or holes) may establish a Fermi–Dirac distribution, characterized by an electron temperature,  $T_{el}$ , before equilibration with the lattice temperature,  $T_{ph}$ , is reached. As the electron heat capacity is typically 1–2 orders of magnitude smaller compared to the lattice,  $T_{el}$  may reach several thousand Kelvin within 1 ps while the lattice remains relatively cold [7]. This concept of separate electron and phonon temperatures provides the basis of the well-known two-temperature model (2TM) [8] and the validity of this picture has been extensively analyzed both by theory and experiment [9–17]. In the experiments, the electron dynamics

✉ Fax: +49-30/8385-6059, E-mail: Lisowski@physik.fu-berlin.de

following optical excitation have been monitored either indirectly by a properly chosen optical response [10, 11, 13, 15] or directly by time-resolved photoemission of the photoexcited electron distribution [12, 17, 18]. From this work, it is now well established that, at early times after photoexcitation, the dynamics are governed by a non-thermal carrier distribution and that a description within the 2TM is appropriate only after electron thermalization is completed. Note that most of these studies have focused on noble metals as model systems and/or thin films to avoid transport effects, which simplifies the analysis.

Beside the fundamental relevance of electron-scattering processes in solids, their dynamics are of particular importance for the understanding of non-adiabatic processes at surfaces. For adsorption of atoms or molecules from the gas phase, it has long been assumed that the energy exchange with the substrate occurs predominantly by excitations of phonons until, very recently, Gergen et al. provided direct evidence for electron-hole pair excitation during adsorption of various weakly bound species [19]. Such non-adiabatic effects are well established for strongly exothermic surface reactions (like the oxidation of alkali metals) and may lead to emission of exoelectrons or chemiluminescence [20]. At metal surfaces, vibrational energy relaxation is dominated by non-adiabatic coupling to electron-hole pair excitation in the substrate [21], which may strongly affect the dynamics of surface reactions [22].

While the above processes all lead to damping of nuclear motions (and corresponding excitations of the electronic system), the reverse process can be induced by optical excitation of energetic (hot) substrate electrons, which may couple to the adsorbate's degrees of freedom [23, 24]. The resulting vibrational excitation of the adsorbate may eventually lead to surface reactions. For excitation with intense femtosecond laser pulses, the high density of non-equilibrium electrons can even lead to multiple electronic excitations and a corresponding high reaction yield in surface femtochemistry, which depends non-linearly on the absorbed laser fluence. The underlying mechanisms have been described in the framework of the DIMET (desorption induced by multiple electronic transitions [25]) or the 'electronic friction' model [23]. In the latter model, the adsorbate's vibrational degree of freedom is non-adiabatically coupled to the transient hot electron distribution, which is usually described within the 2TM, i.e. by a thermalized (hot) Fermi-Dirac distribution. However, as illustrated in Fig. 1, ultra-short laser excitation creates a highly non-thermal, nascent carrier distribution, which thermalizes on a time scale  $\tau_{th}$ , depending on the excitation density. These energetic, non-thermalized electrons may couple to the adsorbate (e.g. by tunneling into unoccupied adsorbate resonances) much more efficiently compared to a thermalized distribution with equal energy density, which affects the measured reaction yield (see e.g. [26]). Knowledge about the temporal evolution of the non-equilibrium electron distribution and its thermalization dynamics is thus of fundamental importance for a detailed understanding of surface femtochemistry. However, most studies in surface femtochemistry have been performed on bulk samples of transition metals (e.g. Pt [26], Pd [27] and Ru [28]) due to their chemical activity. For these metals, detailed studies of the electron thermalization dynam-

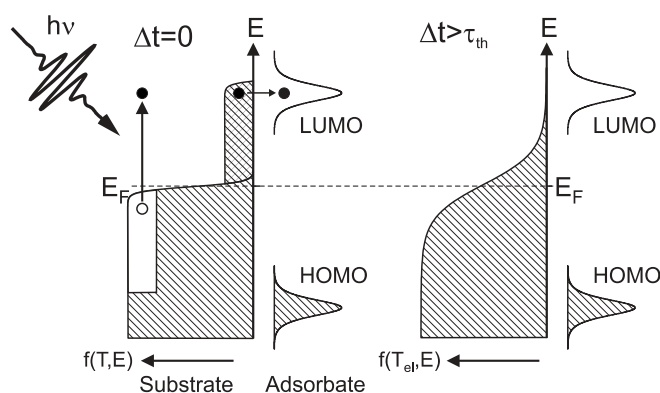


**FIGURE 1** Illustration of the non-equilibrium electron distribution directly after optical excitation of a metal with an ultra-short laser pulse ( $\Delta t = 0$ ) and after development of a thermalized, but still hot Fermi-Dirac distribution ( $\Delta t > \tau_{th}$ ). The higher density of energetic electrons in the non-thermalized distribution may couple more efficiently to unoccupied adsorbate resonances (LUMO), which may strongly influence the reactivity in surface femtochemistry

ics and transport effects are rare [29, 30] and have yet to be performed in a systematic way.

In this paper we investigate the ultra-fast dynamics of electron thermalization and cooling in ruthenium after optical excitation (800-nm, 55-fs laser pulses, absorbed fluence  $\leq 0.6 \text{ mJ cm}^{-2}$ ) directly by time-resolved two-photon photoelectron (2PPE) spectroscopy. We choose Ru(001) as a substrate (also denoted as the hexagonal Ru(0001) surface) because we have previously investigated the surface femtochemistry on this surface for various adsorbates [28, 31]. In the present work, we mainly study  $\text{D}_2\text{O}/\text{Ru}(001)$  due to its reduced work function,  $\Phi$ , compared to bare Ru(001) and probe the entire electron distribution around the Fermi level by a time-delayed probe pulse with a photon energy well above the work function [12, 18]. This allows us to probe the transient non-equilibrium population of both electrons and holes and, thus, the energy density of the excited carriers at the surface. We find that the observed dynamics cannot be described within the 2TM, but can only be accounted for if fast ballistic transport into the bulk and a reduced electron-phonon coupling of non-thermalized electrons are included in an extended model. Both effects lead to a significantly reduced energy density at the surface at later times ( $> 400 \text{ fs}$ ) compared to the predictions of the 2TM. As a consequence, the final temperature after equilibration between electrons and phonons is lower than predicted by the 2TM and, hence, phonon-mediated processes in surface femtochemistry will become less likely.

## 2 Experimental

The electron dynamics at Ru(001) are investigated with a setup combining a tunable femtosecond laser system and an ultra-high vacuum (UHV) chamber for time-resolved two-photon photoemission spectroscopy (see Fig. 2).

The laser system consists of a Ti:sapphire regenerative amplifier (Coherent RegA 9050) pumped by a 10-W diode laser pumped Nd:YVO<sub>4</sub> laser (Coherent Verdi) and seeded by a 30-fs Ti:sapphire oscillator (Coherent Mira). At 200-kHz repetition rate the RegA delivers 800-nm laser pulses with

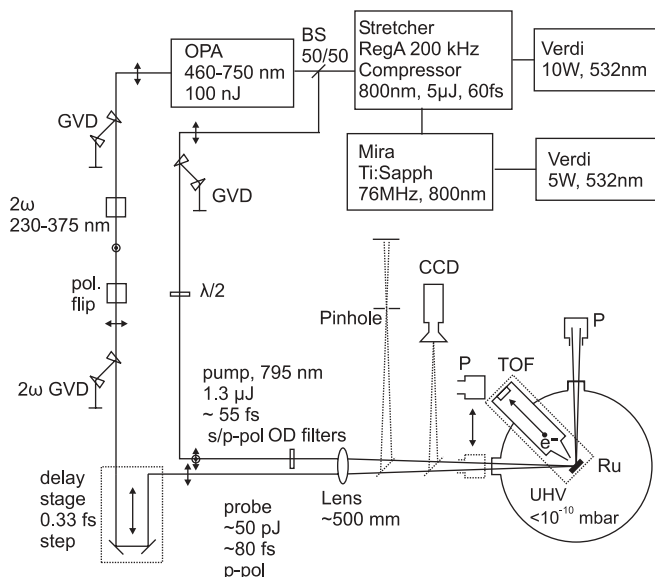


**FIGURE 2** Schematic overview of the experimental setup for time-resolved two-photon-photoemission (2PPE) spectroscopy (see text for details)

a duration of  $\sim 55$  fs (FWHM) and a pulse energy of  $5 \mu\text{J}$ . Half of this output is split off as a pump pulse to excite the Ru sample. The group-velocity dispersion (GVD) is compensated by guiding the beam through a pair of quartz prisms. The (linear) polarization of the 800-nm pump beam is controlled by a  $\lambda/2$  waveplate and its fluence is varied with a set of neutral density filters. The other half of the RegA output pumps an optical parametric amplifier (Coherent OPA 9450) with the signal output ranging from 460 nm to 750 nm with about 100-nJ pulse energy depending on the operation wavelength. The signal of the OPA is first guided through a SF10 prism pair for GVD compensation and is then focused on a 100- $\mu\text{m}$ -thick type-I BBO non-linear crystal to produce a frequency-doubled UV pulse (230–375 nm), which is used to probe the excited-electron distribution. The UV pulses are compressed with a separate pair of quartz prisms and pass a computer-controlled delay stage to set the time delay between pump and probe. Both beams are focused onto the Ru surface with a 50 cm focal length quartz lens. Note that for some 2PPE experiments (as specified in the text) the fundamental of the OPA output ( $h\nu$ ) is used in combination with the frequency-doubled UV pulses ( $2h\nu$ ).

To characterize the pump- and probe-beam profiles at the Ru surface, a mirror can be flipped into the beam path in front of the UHV chamber to image the pump and probe beams onto a CCD camera. The optical path length from the last lens of the optical setup to the CCD camera was set equal to the optical path from the lens to the surface so that we are able to simulate the beam profiles at the focal spot at the sample surface (see Fig. 2).

Both beam profiles exhibit a Gaussian shape, as shown in Fig. 3. The pump-beam diameter was intentionally set wider than the probe to achieve a quasihomogeneous excitation density over the probed area. To ensure spatial overlap of pump and probe, both beams are steered through a 200- $\mu\text{m}$  pinhole, which is positioned at a position equivalent to the sample. The optimum overlap is achieved by maximizing the

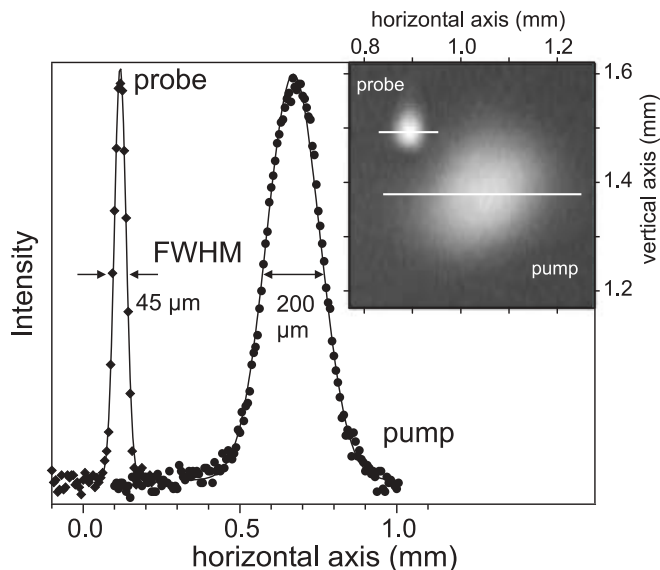


**FIGURE 3** Normalized pump- and probe-beam cross sections at the optical path position of the Ru surface; the *solid lines* are fits of Gaussian distributions. *White lines* in the *inset* depict the lateral intensity distribution; they indicate the line scans given in the main figure. Beams are intentionally displaced for clarity

pump-induced signal. The absorbed fluence was determined from the power reflected by the Ru sample after taking into account the measured transmission coefficients of the chamber's input and output windows. For *s*-polarized light at 800 nm the absorbance of the Ru surface at  $45^\circ$  angle of incidence was found to be 25(2)%, which is in reasonable agreement with a value of 29% calculated from tabulated optical constants ( $\epsilon_1 = 0.8$ ,  $\epsilon_2 = 33.8$  [32]). For the determination of the absorbed fluence, we considered the explicit Gaussian shape of the pump beam intensity profile, as obtained by fitting the measurements in Fig. 3. This intensity is integrated in an area within the FWHM of the probe beam. This approach allows us to calculate the actual absorbed fluence in the probed area only. Thus, from the measured absorbance and beam profile of the pump beam we obtain the absorbed fluences, which in this work are 40, 230 and  $580 \mu\text{J cm}^{-2}$ .<sup>1</sup>

Photoelectrons are detected in an electron time-of-flight (TOF) spectrometer and analyzed according to their kinetic energy  $E_{\text{kin}}$  as well as their momentum  $k_{\parallel}$  parallel to the surface. In the present study, however, we detect photoelectrons only in normal emission ( $k_{\parallel} = 0$ ) within an angular acceptance of the electron TOF spectrometer of  $\pm 3.5^\circ$ . Since the electron's time of flight is measured, the energy resolution of the TOF spectrometer depends on electron energy. In the range of  $E_{\text{kin}} \sim 1$  eV it is better than 10 meV. The pulse duration of the 800-nm pump and the UV probe is determined

<sup>1</sup> Due to the very small pump-induced changes on the 1PPE background it was not possible to maximize the overlap between pump and probe beams for the lowest fluence ( $40 \mu\text{J cm}^{-2}$ ). As insertion of the neutral density filter in the 800-nm path may cause a slight misalignment of the overlap we corrected the value obtained by the CCD camera ( $100 \mu\text{J cm}^{-2}$ ) to  $40 \mu\text{J cm}^{-2}$ , according to the amplitude of the non-thermal part of the spectrum (Fig. 6). This value provides a good relative measure of the absorbed fluence when compared with spectra at higher fluence

by evaluating the 2PPE cross-correlation signal of electrons at 1.4 eV above  $E_F$  on the surface, giving a FWHM below 100 fs for the cross-correlation width. To account for the finite lifetime of electrons at 1.4 eV above  $E_F$  the maximum of the cross-correlation curve was assumed at  $\Delta t = 15$  fs, which is used as a reference for time zero.

The Ru(001) single crystal is mounted in a UHV chamber (base pressure  $< 10^{-10}$  mbar) and is cleaned by cycles of Ar<sup>+</sup> sputtering (700-eV kinetic energy) and heating to 1300 K in an O<sub>2</sub> atmosphere of  $10^{-7}$  mbar for 10 min. Prior to 2PPE measurements, the Ru sample is flashed to 1600 K for 30 s. This preparation leads to a sharp, low-background, low-energy electron diffraction (LEED) pattern and contamination below the sensitivity of Auger-electron spectroscopy (AES). As explained below, in most of the experiments the work function of clean Ru(001) was lowered by adsorption of 1 bilayer (BL) D<sub>2</sub>O at 150 K substrate temperature employing a pin-hole gas doser. The respective coverage was determined by the integrated desorption yield in thermal desorption spectra (TDS).

### 3 Results

A complete analysis of the thermalization and cooling dynamics would require knowledge about the temporal evolution of the entire photoexcited carrier distribution (i.e. of both electrons and holes around  $E_F \pm h\nu_{\text{pump}}$ ). In practice, however, space-charge effects, detector saturation as well as available photon energies limit the accessible energy range for probing photoexcited holes to typically  $\sim 300$ – $400$  meV below  $E_F$ . In the corresponding time-resolved 2PPE experiments, an intense pump pulse ( $h\nu_{\text{pump}}$ ) excites a non-equilibrium carrier distribution and their temporal evolution is probed by a time-delayed UV pulse with photon energy  $h\nu_{\text{probe}}$  well above the sample work function  $\Phi$ . Such a variant of 2PPE spectroscopy has been employed previously to study the electron dynamics around the Fermi level, for example, in thin Au films [12], graphite [18, 33] or Ag clusters on graphite [17]. Here we apply this approach to the Ru(001) surface which has a work function of  $\Phi_{\text{Ru}} = 5.4$  eV. As this energy is close to the limit of the tuning range of our OPA, we have also studied 1 BL of D<sub>2</sub>O/Ru(001), which exhibits a work function of only 4.16 eV. To demonstrate that the water overlayer will not affect the thermalization dynamics close to  $E_F$  we will first briefly discuss the electron dynamics at the D<sub>2</sub>O/Ru(001) interface. A detailed analysis will be subject of a future publication [34].

Figure 4 depicts a photoelectron distribution for 1 BL D<sub>2</sub>O/Ru(001) as a function of pump–probe delay at different intermediate state energies  $E - E_F$  between the Fermi level and the vacuum level ( $E_{\text{vac}}$ ). In contrast to the data presented below, both beams were *p*-polarized ( $h\nu_1 = 2.05$  eV and  $h\nu_2 = 4.1$  eV), which allows us to excite also image potential and adsorbate-induced states. Positive delays  $\Delta t$  account for the UV laser pulse  $h\nu_2$  being delayed with respect to  $h\nu_1$  serving as pump. Negative values account for the opposite (pump with UV, probe with  $h\nu_1$ ). The corresponding processes are shown schematically in the upper panel of Fig. 4. The energy axes represent the intermediate state energy  $E - E_F = E_{\text{kin}} + \Phi - h\nu_{\text{probe}}$  and thus depend on the sign of the de-

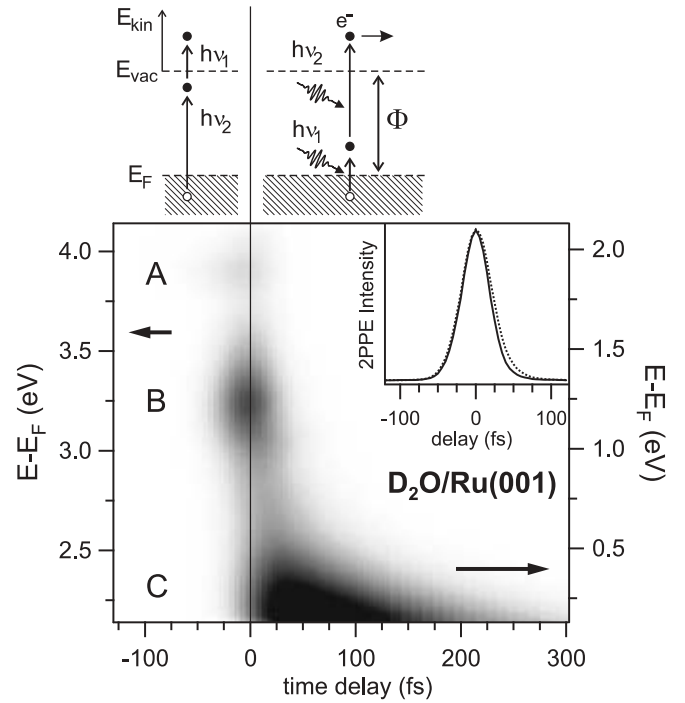


**FIGURE 4** 2PPE intensity (gray scale) at different intermediate-state energies as a function of pump–probe delay measured for 1 BL D<sub>2</sub>O/Ru(001) with  $h\nu_1 = 2.05$  eV and  $h\nu_2 = 4.10$  eV (both *p*-polarized). The intermediate-state energy is calculated according to  $E - E_F = E_{\text{kin}} - h\nu_{\text{probe}} + \Phi$ . For negative delays the excited-electron distribution is probed by  $h\nu_1$  at  $E - E_F$  close to  $E_{\text{vac}}$  (left-hand axis). Since for positive delay the probe photon energy is  $h\nu_2$ , the corresponding intermediate-state energy is 2.05 eV lower (right-hand axis) and represents the energy of excited electrons (C) in Ru(001) near  $E_F$ . Additional peaks arise from the  $n = 1$  (B) and  $n = 2$  (A) image-potential states of D<sub>2</sub>O/Ru(001). The inset shows cross correlations at two energy levels: 3.55 and 3.2 eV above  $E_F$ . The one at 3.2 eV (dotted line) exhibits a slight decay towards positive delay while the 3.5 eV cross correlation (solid line) follows the pump–probe pulse profile

lay, which leads to two energy scales (left and right) given in the figure.

The time-resolved 2PPE spectra in Fig. 4 exhibit three features (A–C): the low-energy feature (C) at  $E - E_F \leq 0.6$  eV and positive delays originates from excited electrons in the Ru substrate and is the focus of the present paper. It corresponds to the scheme in the upper-right of Fig. 4: electrons below  $E_F$  are excited optically by  $h\nu_1 = 2.05$  eV resulting in a non-thermal electron–hole pair distribution as indicated in Fig. 1 (left). The subsequent electron thermalization dynamics observed with increasing delay will be analyzed in detail below. The features (A) and (B) correspond to a 2PPE process depicted in the upper-left of Fig. 4.

Electrons are excited by  $h\nu_2 = 4.1$  eV into the  $n = 1$  (B) and  $n = 2$  (A) image potential states of 1 BL D<sub>2</sub>O/Ru(001) [34], which forms a well-ordered interface at the bilayer coverage [35]. The  $n = 2$  image potential state decays to negative time delays as a consequence of the excitation by  $h\nu_2$ . The inset shows two cross-correlation traces, one taken in a  $\pm 100$ -meV window around 3.55 eV (solid line), which is used to characterize the width of pump and probe pulses and one taken at 3.2 eV (peak B, dotted line). For negative delays both traces are identical, which means that the ultra-fast decay rate of state (B) is not resolved in the experiment and is faster than the laser-pulse duration. The



slight asymmetry of the dotted line towards positive time delay reflects the relaxation of non-equilibrium *d*-band electrons excited by  $h\nu_1$  and probed by  $h\nu_2$ . An influence of the molecular adlayer on the excited-electron dynamics near  $E_F$  can be excluded due to three reasons: (i) the image potential states are the only adsorbate-induced features observed in the 2PPE spectra. They are excited by the UV pulse  $h\nu_2$  and decay at zero or negative delays faster than the experimental time resolution, while electrons near  $E_F$  (C) relax at positive delays. (ii) Moreover, the energetic separation of features B and C and the very low UV photon fluence in comparison to the strong 800-nm pump pulses used below minimizes any further influence. (iii) Both image potential states exhibit  $\sigma$ -symmetry and can only be excited with *p*-polarized light [36]. In all 2PPE experiments shown below we have therefore used *s*-polarized pump pulses (at  $h\nu_1 = 1.55$  eV) to exclude any contributions from multi-photon excitation of surface resonances. Under these conditions we can safely assume that the observed carrier dynamics near  $E_F$  for 1 BL D<sub>2</sub>O/Ru(001) should be identical to bare Ru(001).

As discussed before, adsorption of 1 BL D<sub>2</sub>O on Ru(001) reduces the work function to 4.16 eV, which allows us to probe the carrier dynamics by  $h\nu_2 = 4.58$  eV also below  $E_F$ . This is sketched in Fig. 5, which compares the photoelectron energy distribution before and after ( $\Delta t = 100$  fs) excitation with the *s*-polarized 800-nm pump pulse with an absorbed fluence of  $580 \mu\text{J cm}^{-2}$ . The hatched area shows the equilibrium photoemission spectrum of D<sub>2</sub>O/Ru(001) taken at negative pump-probe delay (i.e. UV probe first). The cutoff of the spectrum at  $E - E_F = -0.4$  eV denotes the lowest detected electron energy corresponding to states below  $E_F$  which are probed by direct photoemission. The upper energy limit of the ‘un-

pumped’ spectrum reflects electrons near  $E_F$  in the tail of the Fermi-distribution function. Because the absorbed fluence of  $h\nu_1$  is roughly four orders of magnitude larger than  $h\nu_2$ , multi-photon excitation by the pump pulse results in a photoelectron background even when the UV probe beam is blocked. This contribution, which depends on the absorbed fluence, can be as high as 10% of the correlated signal and is subtracted in the data analysis.

The spectra in Fig. 5 can be described by a superposition of a non-thermalized electron (and hole) distribution as well as a thermalized part of the electron distribution, which is defined by a Fermi–Dirac distribution  $f(E, T_{\text{el}})$  with a characteristic electron temperature  $T_{\text{el}}$ :

$$f(E, T_{\text{el}}) = \frac{1}{e^{(E-E_F)/k_B T_{\text{el}}} + 1}. \quad (1)$$

To account for spectrometer resolution and energetic bandwidth of the laser pulses,  $f(E, T_{\text{el}})$  is convoluted with a Gaussian of 47 meV FWHM and is then used as a fitting function to the 2PPE spectra as in Fig. 5 in a selected energy interval around  $E_F$ . Different slopes of the falling edge at  $E_F$  denote different temperatures  $T_{\text{el}}$  of the electron gas. The fit of the unpumped spectrum in Fig. 5 represents the equilibrium temperature of the investigated area on the surface, which is 100 K. Note that at  $\Delta t = 100$  fs after excitation, more than 80% of the electron distribution is well described by a Fermi–Dirac distribution with an electron temperature of 225 K (dashed line in Fig. 5). Hereby the fitting was restricted to an energy interval  $-20 \text{ meV} < E - E_F < 80 \text{ meV}$ . However, this thermalized distribution obviously does not account for the total energy in the excited system, as the entire carrier distribution is strongly non-thermal with non-equilibrium hot electrons populating states up to 1.2 eV above  $E_F$ . To extract this fraction of non-thermal carriers from our 2PPE spectra we also approximate the non-thermal part of the electron distribution by a Fermi distribution  $f(E, T_{\text{nt}})$  using an ‘auxiliary temperature’  $T_{\text{nt}}$  (see the appendix). From the amplitude of this non-thermal contribution (solid line in Fig. 5) we obtain that  $\sim 18\%$  of the excited-electron population is non-thermal and is thus not described by  $f(E, T_{\text{el}})$ . The spectra also exhibit signatures of the density of states (DOS) in Ru: while this DOS is rather constant in an interval of  $\pm 1$  eV around  $E_F$  [37] a pronounced peak due to states of mostly *d*-like character appears at 1 eV above  $E_F$  in the DOS, which is also visible in the  $\Delta t = 100$  fs spectrum of Fig. 5.

The time evolution of the non-equilibrium electron distributions between 0 fs and 500 fs are compared in Fig. 6 for three different absorbed pump fluences at an initial sample temperature of 100 K. With increasing fluence we observe an increase of the relative number of non-equilibrium electrons, as well as an increase in the electron temperature of the thermalized Fermi–Dirac distribution. At  $\Delta t = 0$  fs the fraction of non-thermalized electrons and holes is 0.5%, 4% and 9% for a fluence of 40, 230 and  $580 \mu\text{J cm}^{-2}$  respectively. On the other hand the fraction of thermalized carriers decreases with increasing fluence because more electrons are photoexcited and contribute to the strongly non-thermal distribution ranging up to 1.55 eV above  $E_F$ . Note that for all fluences studied the spectrum at  $\Delta t = 100$  fs crosses the one at  $\Delta t = 0$  fs near  $E - E_F = 0.3$  eV. Thus, the number of electron–hole pairs

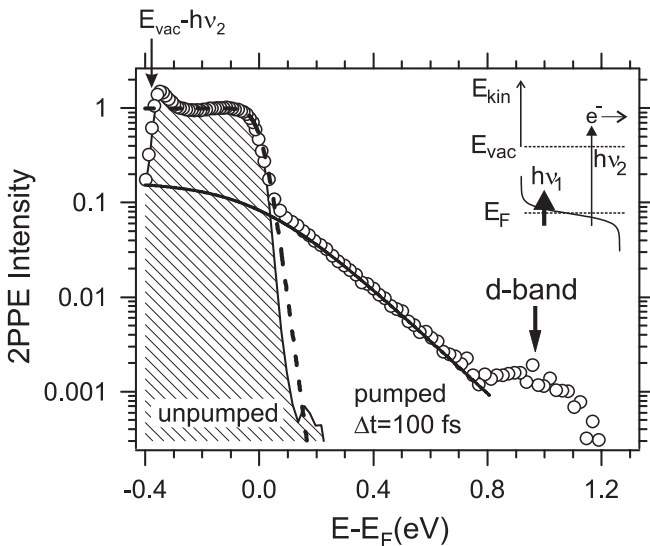


**FIGURE 5** Comparison of pumped ( $\circ$ ,  $\Delta t = 100$  fs, absorbed fluence  $580 \mu\text{J cm}^{-2}$ ) and unpumped (hatched) 2PPE spectra of 1 BL D<sub>2</sub>O/Ru(001) on logarithmic scale (*s*-polarized pump  $h\nu_1 = 1.55$  eV, *p*-polarized probe pulses  $h\nu_2 = 4.58$  eV). The low-energy cutoff at  $E - E_F = -400$  meV occurs because electrons at lower energy cannot be excited above  $E_{\text{vac}}$  by the photon energies used. All spectra are normalized to unity at  $-150$  meV. The *dashed line* indicates a Fermi–Dirac distribution  $f(E, T_{\text{el}})$  with  $T_{\text{el}} = 225$  K fitted to the pumped spectrum in the vicinity of  $E_F$ . The *thick solid line* approximates the non-thermal part of the excited-electron distribution (see text)

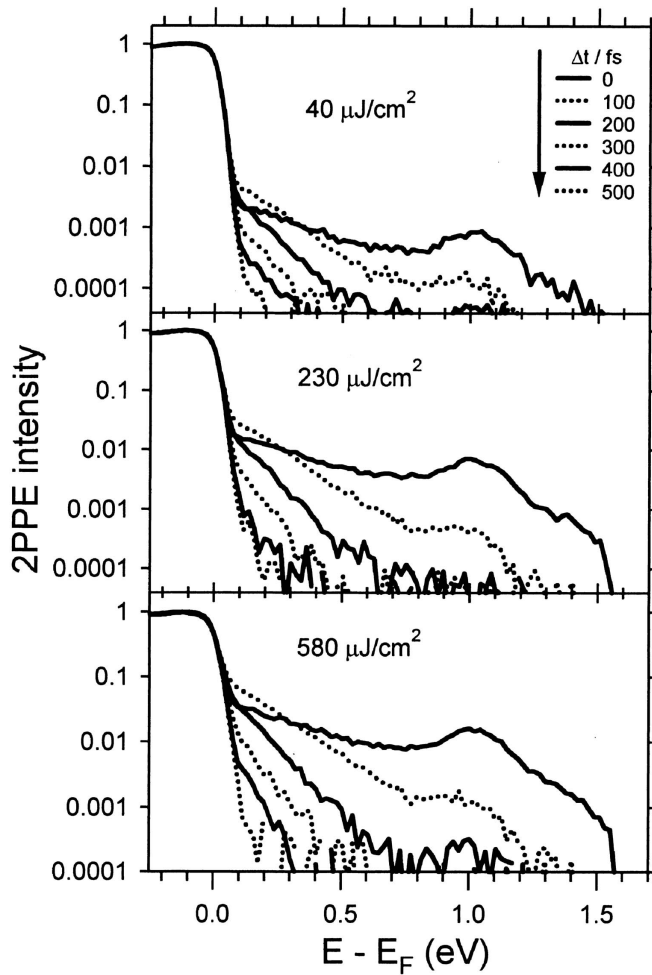


**FIGURE 6** 2PPE spectra (logarithmic intensity scale) for 1 BL D<sub>2</sub>O/Ru(001) versus time delay at the three indicated absorbed fluences, pumped by  $h\nu_1 = 1.55$  eV (*s*-polarized) and probed by  $h\nu_2 = 4.58$  eV (*p*-polarized). Spectra are normalized to unity at  $E - E_F = -150$  meV

increases with time at energies below 0.3 eV and decreases above. At  $\Delta t = 100$  fs the fraction of non-thermal electrons goes through a maximum (18% for the highest pump fluence) and decreases at later times. These population dynamics are mediated by e–e scattering processes leading to thermalization within the electronic system and creation of secondary electron–hole pairs, whereas e–e scattering and energy transport into the bulk leads to energy relaxation and cooling at the surface. In the following, we will discuss the temporal evolution of the energy density in the electronic system, which accounts for both thermalized and non-thermal electrons and holes, and compare it with model predictions.

As our 2PPE scheme probes holes only up to energies of 400 meV below  $E_F$ , we will analyze how far the dynamics of photoexcited holes are identical to electrons with the same energy with respect to  $E_F$ . This approach would allow us to determine the transient energy density of the entire electronic system by analyzing only photoexcited electrons above  $E_F$ . Figure 7 shows time-resolved 2PPE spectra (absorbed fluence  $580 \mu\text{J cm}^{-2}$ ) after subtraction of the unpumped, equilibrium electron distribution obtained from spectra at negative delays (see Fig. 5, hatched spectrum). The pump-induced changes of the electron distribution in Fig. 7 are character-

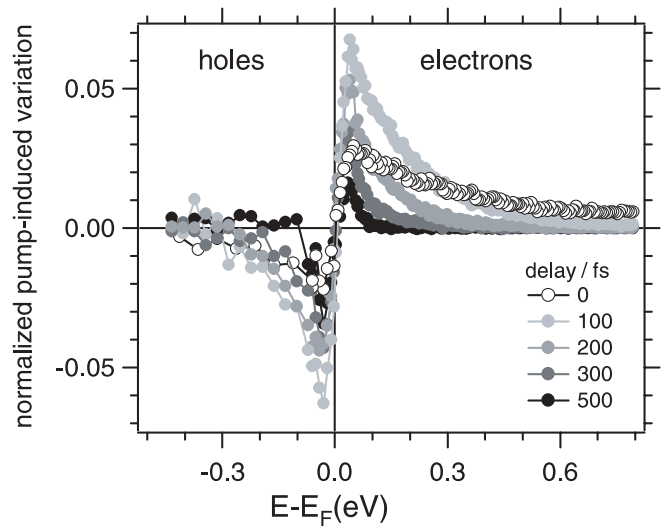


**FIGURE 7** Time evolution of the pump-induced changes of the electron distribution for 1 BL D<sub>2</sub>O/Ru(001) (absorbed fluence  $580 \mu\text{J cm}^{-2}$ ) obtained from data in Fig. 6 after subtraction of the unpumped electron distribution (taken at negative delays)

ized by an increase (decrease) in the population above (below)  $E_F$ . Thereby, the depopulation of states below  $E_F$  by photoexcitation with the pump pulse leads to formation of transient holes [18]. The lower signal to noise ratio at  $E < E_F$  results from background subtraction of the majority of cold electrons below  $E_F$ . At zero delay, the difference spectrum is rather broad compared to later time delays, which reflects the optical excitation of non-thermal electron–hole pairs. Peaks of these difference spectra are located  $\sim 50$  meV above and below  $E_F$  for electrons and holes, respectively. Scattering processes among electrons or holes redistribute the excess energy and increase the carrier population at states closer to  $E_F$ , which leads to crossing of spectra at 0 fs and 100 fs near  $\pm 300$  meV for electrons and holes, respectively. At later time delays, the difference spectra become narrower and lower in amplitude as the excess energy which is initially deposited in the electronic system is transferred out of the detection volume, i.e. into the bulk.

For all time delays the difference spectra in Fig. 7 are anti-symmetric with respect to inversion at  $E = E_F$ , which suggest an equivalence in the dynamics of electrons and holes. This is a consequence of the nearly flat DOS in Ru in the vicinity of  $E_F$  and confirms that the absorbed photon energy is equally distributed among electrons and holes. We will assume in the following that the electron dynamics above  $E_F$  mimic the entire dynamics of holes as well. This assumption is confirmed by Fig. 8, which shows the time evolution of the number of electrons and holes integrated over energy intervals of  $\pm 0.3$  eV around  $E_F$ :

$$n_{\pm}(t) = \int_0^{\pm 0.3 \text{ eV}} N(E, t) dE. \quad (2)$$

We find that both electrons and holes exhibit the same time evolution and from now on we will analyze only the electron dynamics above  $E_F$ . The excess energy density  $U(t)$  in

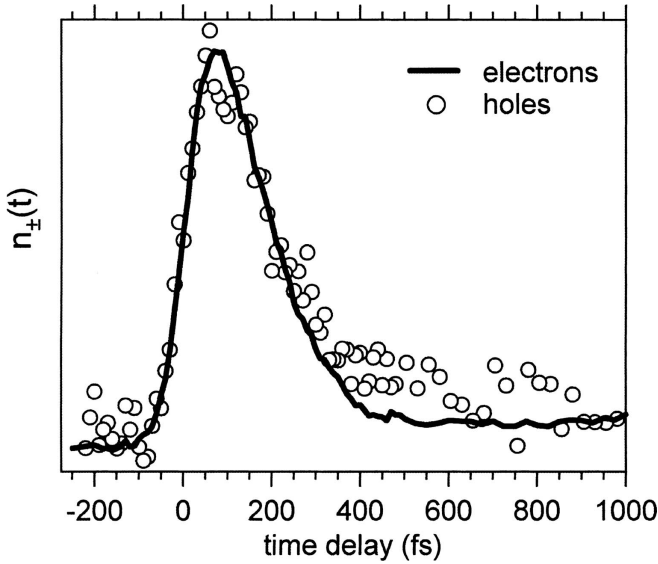


**FIGURE 8** Relative number of photoexcited electrons ( $n_+$ ) and holes ( $n_-$ ) within energy intervals of  $\pm 0.3$  eV around  $E_F$  obtained from the pump-induced changes (cf. Fig. 7) as a function of pump-probe delay (absorbed fluence  $580 \mu\text{J cm}^{-2}$ , 1 BL  $\text{D}_2\text{O}/\text{Ru}(001)$ )

the system is then calculated by integrating the intermediate-state electron energy weighted by the respective population  $N(E, t)$ :

$$U(t) = 2 \int_{E_F=0}^{1.6 \text{ eV}} N(E, t) |E| dE, \quad (3)$$

where the holes contribute by a factor of two to  $U(t)$ . Due to the unknown probed volume and exact fluence of the probe

pulse the energy density is only known up to a constant factor. We have therefore matched the energies derived from our data and the model calculations at negative delays.

The temporal evolution of the energy density  $U(t)$  is plotted in Fig. 9 for clean Ru(001) and for 1 BL  $\text{D}_2\text{O}/\text{Ru}(001)$  on a logarithmic scale. The rise of the energy density occurs on the time scale of the laser-pulse profile since photon absorption occurs only within the laser-pulse duration. The transient changes of  $U(t)$  are comparable to that of the electron population (Fig. 8) and occur on a time scale of only 400 fs. This has to be compared with the much slower response times observed for noble metals of typically 1–2 ps [7, 12]. The most striking result is, however, that after 500 fs the energy density at the surface drops nearly to the same value as before excitation. As will be discussed in detail below, this indicates that most of the absorbed energy is carried away by efficient transport from the surface into the bulk. Note also that this finding is observed for both clean and  $\text{D}_2\text{O}$ -covered Ru(001), which reveals that the adsorbate layer does not influence the electron dynamics.

Furthermore, it is possible to extract from the electron spectra the non-thermalized contribution (see Fig. 5) and calculate the transient energy density  $U_{nt}(t)$  of non-thermalized electrons. We find that  $U_{nt}(t)$  of the non-thermalized electrons decays exponentially with time constants of 96, 66 and 75 fs for the pump fluences of 40, 230 and  $580 \mu\text{J cm}^{-2}$ , respectively. The latter two values are nearly identical within the error bars ( $\pm 5$  fs) whereas for the lowest pump fluence the decay time is significantly longer. Therefore, a trend of decreasing decay time with increasing pump fluence seems evident. Note that one cannot simply identify these decay times with thermalization times because energy loss of the non-thermalized electrons occurs also due to transport and e-ph coupling. We also analyzed the decay time of the population

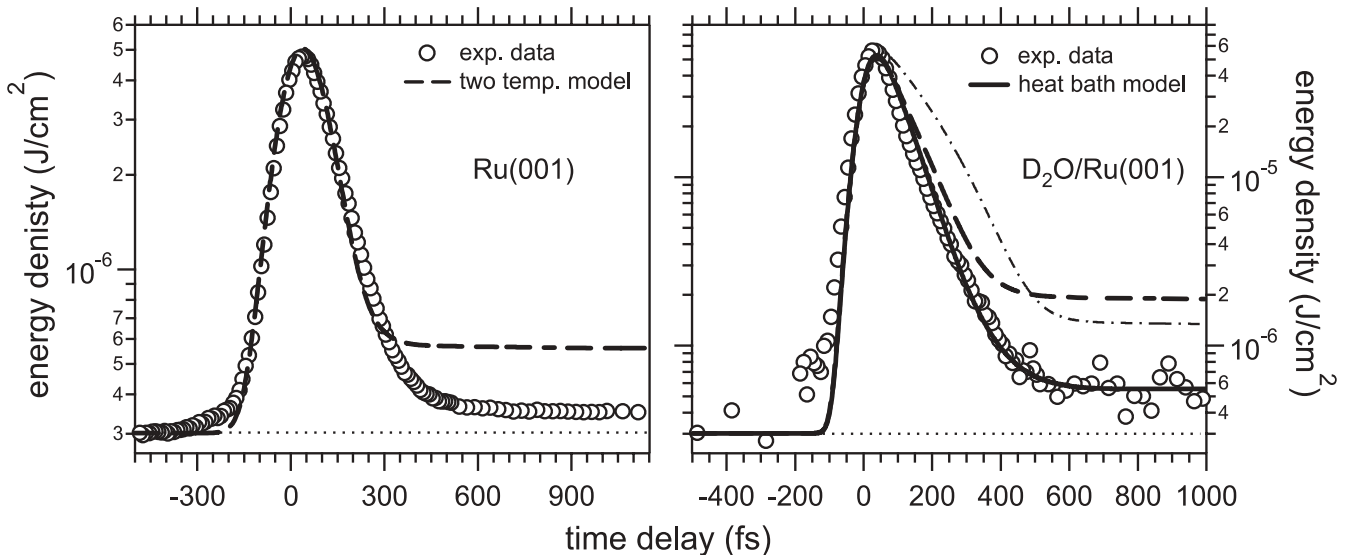


**FIGURE 9** Temporal evolution of the energy density  $U(t)$  at the bare Ru(001) surface (left, absorbed fluence of  $250 \mu\text{J cm}^{-2}$ ) and for 1 BL  $\text{D}_2\text{O}/\text{Ru}(001)$  (right, absorbed fluence of  $580 \mu\text{J cm}^{-2}$ ). The dashed lines are derived from the 2TM by calculating  $U(t) = c_{el} T_{el}/2$  (where  $c_{el} = \gamma T_{el}$  with  $\gamma = 400 \text{ J m}^{-3} \text{ K}^{-2}$ , see the appendix). The black solid line (right) is the result of an extended heat-bath model accounting for ballistic electron transport and reduced e-ph coupling of non-thermal electrons (see text). For comparison the dash-dotted line (right) shows the result of this model assuming the same e-ph coupling and diffusive transport for all electrons. The thin dashed line (right) is the pump-probe cross-correlation curve indicating the time resolution of our experiment. Note the larger pulse width for bare Ru(001) (cross correlation FWHM of 146 fs for Ru(001) and 92 fs for 1 BL  $\text{D}_2\text{O}/\text{Ru}(001)$ )

of non-thermal electrons, i.e. the deviation from a Fermi–Dirac distribution  $f(E, T_{el})$  [33]. Using this definition for a thermalization time we obtain 140, 113 and 111 fs for the above fluences. In any case, we observe a decrease in the thermalization times with increasing fluence, which is in qualitative agreement with previous observations [12].

Because a good knowledge of the dynamics of energy flow is crucial in applications like femtochemistry, various theoretical or phenomenological approaches have been developed to model these dynamics. In the next section we will therefore try to describe the observed dynamics with a simple phenomenological model.

#### 4 Discussion

As a starting point of our discussion we will first compare the results described above with predictions of the 2TM [8]. We use this model in a refined version published previously [11, 29], which is described in the appendix. It is known that the 2TM is not suitable to describe the full dynamics of the photoexcited electron distribution because it is not possible to attribute a well-defined Fermi–Dirac temperature at early times ( $\Delta t < 400$  fs, see Fig. 6). Therefore, we focus on the energy density in the electron system, which is well defined at all times for both thermal and non-thermal distributions. The electron temperatures obtained by the 2TM are converted to energy using the electron heat capacity  $U_{el} = C_{el}T_{el}/2 = \gamma T_{el}^2/2$ , while the actually measured energy in the electron system is extracted using (3). In order to account for the finite time resolution in the experiment, the simulations are convoluted with a Gaussian according to the probe-pulse duration.

Figure 9 shows the comparison of the energy density  $U(t)$  calculated from the 2TM (thick dashed line) with  $U(t)$  extracted from the data (circles). While at early times ( $\Delta t < 300$  fs) the 2TM provides a fairly good description of the dynamics, there are pronounced deviations for  $\Delta t > 400$  fs: the energy density drops to a significantly lower value than predicted, only slightly above the level before excitation. This means that most of the absorbed energy from the laser pulse must have rapidly dissipated from the surface into the bulk and is not stored by the lattice. An analogous result is found for the transient electron temperature  $T_{el}$  determined from the fit of the thermalized part of the electron distribution (Fig. 10, circles). In the experiment we observe a rise of the electron temperature from 100 K before excitation to 225 K at the peak and finally  $T_{el} = 135$  K at 1 ps, while the 2TM predicts a peak temperature  $T_{el} = 1300$  K and a final value of 250 K. For lower fluences such discrepancies are observed as well, though not as pronounced (not shown). It is not possible to achieve agreement between the 2TM and our data at all times by changing material parameters in a reasonable range<sup>2</sup>. Therefore the dynamics of energy flow must be different than assumed in the 2TM.

In general, the energy density at the surface is a result of the competition of e–ph coupling that localizes the energy

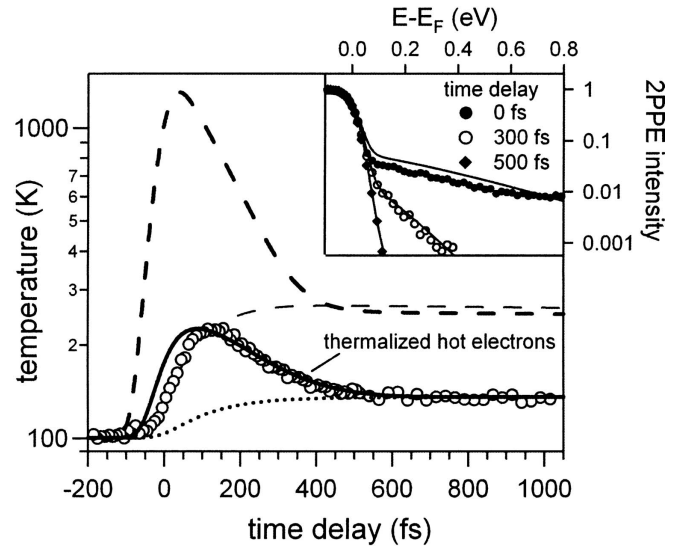


**FIGURE 10** Time evolution of electron temperature (thick dashed line) and lattice temperature (thin dashed line) at the surface for the two-temperature model. For the extended heat-bath model the thermal electron temperature (thick line) and the lattice temperature (dotted line) are shown. Temperatures determined from a fit of Fermi–Dirac functions to the thermal part of the electron spectra are shown as circles. The inset shows electron spectra data at indicated delays and corresponding electron spectra computed from temperatures of the extended heat-bath model as lines

at the surface and heat transport that carries the energy into the bulk. To open up new channels for the dynamics of energy flow we propose an extended heat-bath model, which models the non-thermal electrons in a separate bath. Figure 11 illustrates the energy flow in Ru according to this model: the energy from the laser pulse is injected into the non-thermal electrons (and holes). Due to their high excess energy these carriers exhibit very efficient ballistic and diffusive transport. As the excess energy in the non-thermal bath is distributed over a smaller number of particles compared to a thermalized

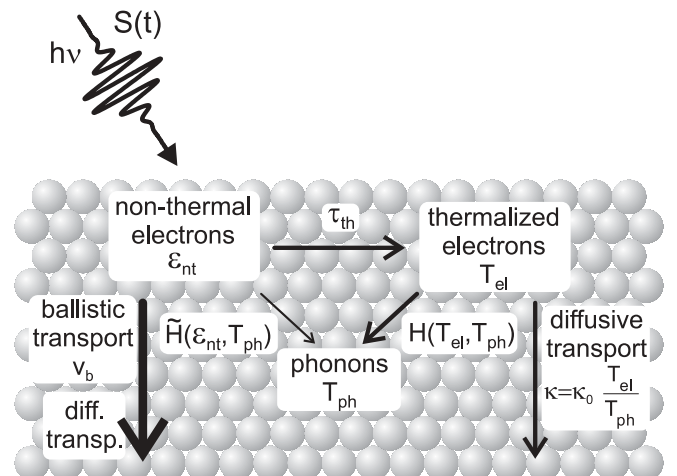


**FIGURE 11** Schematic representation of energy flow in a metal after femtosecond optical excitation (extended heat-bath model). The electron system is split into a non-thermal and a thermal bath, coupled with different strengths to the phonon bath. Energy in the non-thermal bath relaxes with a time constant  $\tau_{th}$  to the thermal bath. Heat transport is modeled as diffusive with a diffusivity of  $\kappa = \kappa_0 T_{el}/T_{ph}$  and for the non-thermal bath as ballistic transport with velocity  $v_b$

<sup>2</sup> A physically unreasonable increase of the lattice heat capacity by a factor of four together with a 10% decrease of the e–ph coupling constant leads formally to agreement of  $U(t)$  derived by the 2TM



bath with the same energy density, the e–ph scattering rate will be reduced. Due to the competition with energy transport into the bulk a small amount of energy is transferred to the thermalized electron bath, which has the same e–ph coupling and transport properties as used in the 2TM above.

Let us now discuss in more detail the individual parts of the model. The extension of the 2TM model is to split the electron bath into two parts, one contribution consisting of thermalized electrons and the second consisting of non-thermal electrons. As we show in the Appendix, this corresponds to two electron baths with separate densities: a high-density bath of thermal electrons and a low-density non-thermal bath. The electron distribution of the thermal bath is described by a Fermi–Dirac distribution, represented by a temperature  $T_{\text{el}}$ . Surprisingly, it is also possible to describe the non-thermal part of the spectra by a Fermi–Dirac distribution (see Fig. 5 and the Appendix); therefore we can formally characterize the non-thermal bath by an ‘auxiliary temperature’  $T_{\text{nt}}$  where necessary. However, as far as possible, we describe the non-thermal bath by its energy density  $U_{\text{nt}}$ . Since the non-thermal electrons are initially created by the pump pulse, this pulse is described by a source term  $S(z, t)$  which acts on the non-thermal bath only. During the first few hundred femtoseconds the non-thermal electrons will acquire a thermal distribution due to e–e scattering. This process is modeled by a coupling which is transferring energy from the non-thermal to the thermal electron bath with a time constant  $\tau_{\text{th}}$ . The non-thermal electrons are initially distributed inhomogeneously in the metal giving rise to ballistic transport with velocity  $v_b$ , which means a net motion of electrons towards non-excited spatial regions. Elastic reflection of ballistic electrons at the surface and the gradient in the excitation density result in a fast net energy transport in the non-thermal bath towards the bulk. Diffusive transport for both electron baths, thermal and non-thermal, is modeled with a temperature-dependent diffusivity  $\kappa = \kappa_0 T_{\text{el}} / T_{\text{ph}}$ . Electron–phonon coupling is modeled by a coupling term,  $H(T_{\text{el}}, T_{\text{ph}})$ , for the thermal and  $\tilde{H}(T_{\text{nt}}, T_{\text{ph}})$  for the non-thermal bath, derived by Kaganov et al. [38]. Since the latter differs from the first only by a constant factor, tuning of the e–ph coupling for both baths is possible.

Figure 9 shows the results of the extended heat-bath model for two parameter sets. The bold line describes the data reasonably well and considers ballistic transport with a velocity  $v_b = 8 \times 10^5 \text{ m s}^{-1}$  and reduced e–ph coupling of non-thermal electrons to 20% of the value used in the 2TM. On the contrary, without ballistic transport (i.e. diffusive transport only) and with identical e–ph coupling for both electron baths, the experimentally observed energy transient is not well described, as shown by the dash-dotted line. The dependence of the diffusivity  $\kappa$  on  $T_{\text{el}}$  should in principle increase transport efficiency for the non-thermal bath even without ballistic transport. However, it turns out that even for the high auxiliary temperatures  $T_{\text{nt}}$  of up to 3500 K the transport is still too weak to explain the data due to a low temperature gradient at the surface. We conclude from these simulations that the electron dynamics at the Ru(001) surface are strongly influenced by ultra-fast (mainly ballistic) energy transport into the bulk, which cannot be accounted for by any reasonable model which considers only diffusive transport (as in the 2TM). Neg-

lecting these transport effects leads to overestimation of the final surface temperature of the system. Our results also suggest that the e–ph scattering rate is reduced compared to a thermalized electron distribution. The phonon-emission rate will be influenced both by the number of excited hot electrons as well as DOS effects. We believe, however, that our data does not allow us to draw further conclusions. A detailed study of the temperature dependence would be beneficial.

Our model describes not only the overall energy transient in the electron system, but also the temperature of thermalized electrons (Fig. 10, thick line). Thus, by inserting temperatures from the model into (A2), electron distributions can be simulated, as seen in the inset of Fig. 10. The result of a rather weak e–ph coupling of non-thermal electrons is already indicated by the lattice-temperature evolution in the 2TM (thin dashed line, Fig. 10): obviously, the lattice temperature exceeds the experimentally determined equilibrium value of 135 K already after a few tens of femtoseconds. Due to the high lattice heat capacity, once energy is deposited in the lattice, it cannot be dissipated in metals on a sub-picosecond time scale, because significant heat transport only takes place through the electron system. The conclusion is that in our experiment the lattice temperature cannot at any time be significantly higher than 135 K, which is indeed reproduced by our extended model (dotted line in Fig. 10).

Although the presented model indeed gives a fairly good description for the energy density and temperature dynamics of the studied system, we do not intend to propose it as a full description of the carrier dynamics, which would require a more fundamental theoretical approach. However, we believe that it provides a good starting point to understand the main physical mechanisms and their interplay in shaping the system’s early dynamics, which are of fundamental interest for femtochemistry.

Finally, we discuss the consequences for surface femtochemistry and related non-adiabatic processes at surfaces [23, 24]. As pointed out in the introduction, photoinduced surface reactions are often mediated by charge-transfer processes of hot electrons (holes) into normally unoccupied (occupied) adsorbate resonances (see Fig. 1). For a given resonance lifetime and excited-state potential energy surface the reaction yield is then governed by the density of excited carriers in the energy interval of the adsorbate resonance (which is typically located around 1–3 eV above  $E_F$  [28, 34]). However, as demonstrated in this and related work, most of the photoexcited electron distribution in this energy range consists of non-thermalized hot electrons, which implies that a description within the 2TM cannot be adequate. This raises the question why the frequently used electronic friction models, which are based on the 2TM to describe the substrate electron dynamics, provide very good agreement for various surface femtochemical processes [23, 24, 28]. The present work on Ru shows that the non-thermal part of the electron distribution ( $\sim 20\%$  for the highest fluence) can be – to a good approximation – effectively described by a Fermi distribution with an ‘auxiliary temperature’  $T_{\text{nt}}$ . Since in typical femtochemistry experiments the absorbed fluence is at least 5–10 times larger compared to our photoemission measurements, essentially all valence electrons around the Fermi level will be excited by the intense pump pulse. As the e–e scattering rate within the

photoexcited electron gas will strongly increase for higher excitation densities, the distinction between the thermalized and non-thermal carrier distributions will become irrelevant and even at early times the electronic system may again be described by an effective electron temperature. However, at such high excitation densities only optical techniques are applicable, as photoelectron spectroscopy becomes impossible due to space-charge broadening.

## 5 Conclusion

Time-resolved two-photon photoelectron spectroscopy was employed to analyze the transient electron and hole distributions following optical excitation of a Ru(001) surface. The experiments were performed with 800-nm pump pulses for absorbed fluences between 0.04 and 0.6 mJ cm<sup>-2</sup>. Transient changes of the electron distribution occur essentially within the first 500 fs (i.e. much faster compared to noble metals), while at later times electrons and phonons are in equilibrium. Within the first 0.5 ps the data show strongly non-thermal electron and hole distributions, making a description by a Fermi–Dirac distribution with a well-defined electron temperature inadequate. However, the dynamics of electrons and holes were found to be identical in an energy interval  $\pm 0.3$  eV around  $E_F$ . Thus, we pursue a description of the dynamics that is based on the energy density of the non-equilibrium electrons only, rather than an electron temperature as used in the 2TM. Apart from the known inability of the 2TM to describe the initial carrier dynamics due to their non-thermal character, we show that it yields an energy density which is systematically too high for time delays  $> 400$  fs. For the maximum fluence used (580  $\mu\text{J cm}^{-2}$ ) this results in an temperature rise of  $\Delta t = 35$  K, while the 2TM would predict a much higher value of  $\Delta t = 150$  K. With the additional insertion of a separate, non-equilibrium bath and the incorporation of a ballistic transport mechanism in the non-thermal electron subsystem, we show that our numerical calculations agree well with the experiment. Therefore, we propose ballistic transport to account for the very efficient energy transfer into the bulk of the metal. In addition electron–phonon coupling for the non-thermal electrons is reduced compared to thermalized electrons.

**ACKNOWLEDGEMENTS** We thank G. Moos and D.N. Denzler for valuable discussions and acknowledge funding by the Deutsche Forschungsgemeinschaft through SPP 1093 and Sfb 290.

## Appendix

In this section the modified heat-bath model is discussed in detail. Our model is based on the 2TM, which is described by the differential equations [11]:

$$C_{\text{el}} \frac{\partial T_{\text{el}}}{\partial t} = \frac{\partial}{\partial z} \left( \kappa \frac{\partial T_{\text{el}}}{\partial z} \right) - H(T_{\text{el}}, T_{\text{ph}}) + S(z, t), \quad (\text{A.1a})$$

$$C_{\text{ph}} \frac{\partial T_{\text{ph}}}{\partial t} = H(T_{\text{el}}, T_{\text{ph}}). \quad (\text{A.1b})$$

The first equation describes the energy balance in the electron bath with (i) electron diffusion ( $\kappa$  is the electron thermal

conductivity), (ii) e–ph coupling  $H$  and (iii) optical excitation with the absorbed energy density per time  $S(z, t)$ . The second equation describes the energy balance in the phonon bath, which is given by the e–ph coupling.

The main idea of our extended model is to split the bath of the electrons into two separate ones: one bath consisting of thermalized electrons and the second one consisting of non-thermal electrons (see Fig. 11). The relative fraction of these two contributions is described by a time- and space-dependent, dimensionless factor  $r(t, z)$ . The relative density of the thermal bath is  $(1 - r)$  while the relative density of the non-thermal bath is  $r$ . Therefore, for the electron baths the conduction-band electron density  $\varrho$  has to be substituted by the reduced density  $(1 - r)\varrho$  for the thermal bath and  $r\varrho$  for the non-thermal bath.

Concerning the distribution functions, it is clear that the thermal electrons are described by a Fermi–Dirac function, while for non-thermal electrons there is a priori no simple expression. However, we found empirically that the distribution function of the non-thermal electrons can be approximated fairly well by a Fermi–Dirac function with reduced amplitude and an auxiliary temperature  $T_{\text{nt}}$  (cf. Figure 5). We do not suggest to understand  $T_{\text{nt}}$  as a real temperature of a system in thermal equilibrium, but rather want to exploit the fact that a Fermi–Dirac function describes the non-thermal part of the measured electron spectra fairly well (cf. Figure 5). Therefore, even for the non-thermal electrons, we can use formulae for e–ph coupling and thermal diffusion that assume a thermal electron distribution. Apart from that, we describe the non-thermal bath in terms of its energy content, which is proportional to  $T_{\text{nt}}^2$ , cf. (A.4). The measured electron spectra can then be described in the following way:

$$N(E) = [(1 - r)f(E, T_{\text{el}}) + rf(E, T_{\text{nt}})]\text{DOS}(E). \quad (\text{A.2})$$

By fitting this distribution  $N(E)$  to observed electron spectra at different time delays we can extract  $r(t, z = 0)$  and  $T_{\text{nt}}(t, z = 0)$ , i.e. the relative density and auxiliary temperature  $T_{\text{nt}}$  of the non-thermal bath at the surface ( $z = 0$ ). We find that  $r$  rises from 0 to a maximum of 0.18 at  $t = 100$  fs for the highest pump fluence (see Fig. 5). The spatial profile of  $r$  is assumed to follow an exponential decay with the optical penetration depth of 16.2 nm [39] because the creation of non-thermal electrons is proportional to the photon density. The density of states  $\text{DOS}(E)$  is assumed to be constant, which is supported by band-structure calculations [37] for an interval of 1 eV centered on  $E_F$ .

We extend the 2TM by splitting the electron system into two parts. Thus, we arrive at a set of three differential equations:

$$\frac{dU_{\text{nt}}}{dt} = \frac{\partial}{\partial z} \left( r\kappa \frac{\partial T_{\text{nt}}}{\partial z} \right) - r\tilde{H}(T_{\text{nt}}, T_{\text{ph}}) - E_{\text{therm}} + S(z, t), \quad (\text{A.3a})$$

$$(1 - r)C_{\text{el}} \frac{\partial T_{\text{el}}}{\partial t} = \frac{\partial}{\partial z} \left( (1 - r)\kappa \frac{\partial T_{\text{el}}}{\partial z} \right) - (1 - r)H(T_{\text{el}}, T_{\text{ph}}) + E_{\text{therm}}, \quad (\text{A.3b})$$

$$C_{\text{ph}} \frac{\partial T_{\text{ph}}}{\partial t} = (1 - r)H(T_{\text{el}}, T_{\text{ph}}) + r\tilde{H}(T_{\text{nt}}, T_{\text{ph}}). \quad (\text{A.3c})$$

The first equation describes the energy balance in the non-thermal electron bath, the second equation the thermal electron bath, while the last equation describes the phonon bath. All physical quantities that are proportional to the electron density are multiplied by a factor of  $r$  or  $(1 - r)$  to account for the splitting of the electron system into two subsystems. As the highly non-thermal electrons are created by the light pulse, the optical excitation term  $S(z, t)$  appears in the equation for the non-thermal electrons only. It has a Gaussian time profile and an exponential decay into the bulk with the optical penetration depth. The e-ph coupling function for the non-thermal electrons,  $\tilde{H}$ , includes a constant factor to control the coupling strength. An additional term  $E_{\text{therm}}$  describes the coupling between both electron baths, thereby modeling processes due to e-e interaction, i.e. thermalization.

The energies of the thermal and non-thermal electrons are given by

$$U_{\text{el}} = \frac{1}{2}(1 - r)\gamma T_{\text{el}}^2, \quad U_{\text{nt}} = \frac{1}{2}r\gamma T_{\text{nt}}^2, \quad U_{\text{el}}^{\text{tot}} = U_{\text{el}} + U_{\text{nt}}, \quad (\text{A.4})$$

where  $\gamma = 400 \text{ J m}^{-3} \text{ K}^{-2}$  is the electronic heat capacity coefficient for Ru [40]. Here we used the linear dependence of the electron heat capacity  $C_{\text{el}}$  on temperature:

$$C_{\text{el}} = \gamma T_{\text{el}}. \quad (\text{A.5})$$

The electron thermal conductivity  $\kappa$  is taken as temperature dependent [29]:  $\kappa(T_{\text{e}}) = \kappa_0 T_{\text{el}}/T_{\text{ph}}$  with  $\kappa_0 = 117 \text{ W m}^{-1} \text{ K}^{-1}$ . The e-ph coupling is modeled with an energy-transfer rate  $H(T_{\text{el}}, T_{\text{ph}})$  that was derived by Kaganov et al. [38] by summation of all one-phonon emission and absorption processes assuming thermal electron (Fermi-Dirac) and thermal phonon (Bose-Einstein) distributions. It has the form  $H(T_{\text{el}}, T_{\text{ph}}) = f(T_{\text{el}}) - f(T_{\text{ph}})$ , where

$$f(T) = 4gT \left( \frac{T}{\Theta_{\text{D}}} \right)^4 \int_0^{\Theta_{\text{D}}/T} \frac{x^4}{e^x - 1} dx, \quad (\text{A.6})$$

with the e-ph coupling constant  $g = 1.85 \times 10^{18} \text{ W m}^{-3} \text{ K}^{-1}$  [29] and the Debye temperature  $\Theta_{\text{D}} = 404 \text{ K}$  [41]. The temperature dependence of the lattice heat capacity  $C_{\text{ph}}$  is described using the Debye approximation with a high-temperature value of  $C_{\text{ph}}(T \rightarrow \infty) = 24.943 \text{ J mol}^{-1} \text{ K}^{-1}$ .

The thermalization of the electron gas leads to two phenomena visible in the measured electron spectra (Fig. 6): in the initial stages of thermalization a large number of moderately high energetic electrons are created by scattering with high energetic electrons. This leads to the visible intensity rise for  $E - E_{\text{F}} = 0$  to  $0.3 \text{ eV}$  for the first 100 fs, which is modeled by a rising  $r(t)$ , since the shape of the spectra suggests counting these electrons to the non-thermal bath. In principle, this can be viewed as an internal thermalization of the non-thermal electrons. Second, inspection of the electron energy in the non-thermal part of the spectra shows that this energy is at the same time decaying exponentially. To account for this fact, the coupling term  $E_{\text{therm}}$  between the two electron baths is proportional to the energy difference in the two electronic

subsystems with a time constant  $\tau_{\text{th}}$ :

$$E_{\text{therm}} = \gamma(T_{\text{nt}}^2 - T_{\text{el}}^2)/\tau_{\text{th}}. \quad (\text{A.7})$$

For the non-thermal electrons we have implemented a simple mechanism for ballistic transport. We assume an isotropic initial velocity with  $v_{\text{b}} = 8 \times 10^5 \text{ m s}^{-1}$  upon excitation, which is justified by the roughly spherical shape of large parts of the Fermi surface [42]. This value of  $v_{\text{b}}$  is in agreement with the Fermi velocity  $v_{\text{F}} = dE/dk = 10^6 \text{ m s}^{-1}$  and  $5 \times 10^5 \text{ m s}^{-1}$  for the two bands along  $\Gamma A$ , determined from recent band-structure calculations [37]. We consider only the component of the velocity vector normal to the surface. During the summation, we keep note of the relative number of electrons propagating towards and away from the surface and implement a reflection of ballistic electrons at the surface.

The model calculations are done by integrating the differential equations (A.3a)–(A.3c), with time steps of  $10^{-17} \text{ s}$  on a one-dimensional grid with 1-nm spacing. To account for the small escape depth of photoexcited electrons, only the energy and temperature from the top 1 nm are used for comparison with experimental data.

## REFERENCES

- 1 P. Drude: Ann. Phys. (Leipzig) **1**, 566 (1900)
- 2 M. Kaveh, N. Wisner: Adv. Phys. **33**, 257 (1984)
- 3 J. Shah: *Ultrafast Spectroscopy of Semiconductors and Semiconductor Nanostructures*, 2nd edn. (Springer, Berlin 1999)
- 4 P.M. Echenique, J.M. Pitarke, E.V. Chulkov, A. Rubio: Chem. Phys. **251**, 1 (2000)
- 5 D. Pines, P. Nozieres: *The Theory of Quantum Liquids* (Benjamin, New York 1966)
- 6 H. Petek, S. Ogawa: Prog. Surf. Sci. **56**, 239 (1997)
- 7 N. Del Fatti, C. Voisin, M. Achermann, S. Tzotzakakis, D. Christofilos, F. Vallée: Phys. Rev. B **61**, 16956 (2000)
- 8 S.I. Anisimov, B.L. Kapeliovich, T.L. Perel'man: Sov. Phys. JETP **39**, 375 (1974)
- 9 H.E. Elsayed-Ali, T.B. Norris, M.A. Pessot, G.A. Mourou: Phys. Rev. Lett. **58**, 1212 (1987)
- 10 R.W. Schoenlein, W.Z. Lin, J.G. Fujimoto, G.L. Eesley: Phys. Rev. Lett. **58**, 1680 (1987)
- 11 R.H.M. Groeneveld, R. Sprik, A. Lagendijk: Phys. Rev. B **51**, 11433 (1995)
- 12 W.S. Fann, R. Storz, H.W.K. Tom, J. Bokor: Phys. Rev. Lett. **68**, 2834 (1992); Phys. Rev. B **46**, 13592 (1992)
- 13 C.-K. Sun, F. Vallée, L.H. Acioli, E.P. Ippen, J.G. Fujimoto: Phys. Rev. B **50**, 15337 (1994)
- 14 V.E. Gusev, O.B. Wright: Phys. Rev. B **57**, 2878 (1998)
- 15 J. Hohlfeld, S.-S. Wellershoff, J. Güdde, U. Conrad, V. Jähnke, E. Matthias: Chem. Phys. **251**, 237 (2000)
- 16 B. Rethfeld, A. Kaiser, M. Vicanek, G. Simon: Phys. Rev. B **65**, 214303 (2002)
- 17 M. Merschdorf, C. Kennerknecht, K. Willig, W. Pfeiffer: New J. Phys. **4**, 95 (2002)
- 18 G. Moos, C. Gahl, R. Fasel, M. Wolf, T. Hertel: Phys. Rev. Lett. **87**, 267402 (2001)
- 19 G. Gergen, H. Nienhaus, W.H. Weinberg, E.W. McFarland: Science **294**, 2521 (2001)
- 20 T. Greber: Surf. Sci. Rep. **28**, 3 (1997)
- 21 B.N.J. Persson, M. Persson: Solid State Commun. **36**, 175 (1980)
- 22 L. Diekhöner, L. Hornekaer, H. Mortensen, E. Jensen, A. Baurichter, V.V. Petrunin, A. Luntz: J. Chem. Phys. **117**, 5018 (2002)
- 23 M. Brandbyge, P. Hedegard, T.F. Heinz, J.A. Misewich, D.N. Newns: Phys. Rev. B **52**, 6042 (1995)
- 24 R.R. Cavanagh, D.S. King, J.C. Stephenson, T.F. Heinz: J. Chem. Phys. **97**, 786 (1993)
- 25 J.A. Misewich, T.F. Heinz, D.M. Newns: Phys. Rev. Lett. **68**, 3737 (1992)

- 26 S. Deliwala, R.J. Finlay, J.R. Goldman, T.H. Her, W.D. Mieber, E. Mazur: *Chem. Phys. Lett.* **242**, 617 (1995)
- 27 J.A. Misewich, S. Nakabayashi, P. Weigand, M. Wolf, T.F. Heinz: *Surf. Sci.* **363**, 204 (1996)
- 28 M. Bonn, S. Funk, Ch. Hess, D.N. Denzler, C. Stampfl, M. Scheffler, M. Wolf, G. Ertl: *Science* **285**, 1042 (1999)
- 29 M. Bonn, D.N. Denzler, S. Funk, M. Wolf, S.-S. Wellershoff, J. Hohlfeld: *Phys. Rev. B* **61**, 1101 (2000)
- 30 C. Lei, M. Bauer, K. Read, R. Tobey, Y. Liu, T. Popmintchev, M.M. Murnane, H.C. Kapteyn: *Phys. Rev. B* **66**, 245 420 (2002)
- 31 D.N. Denzler, Ch. Hess, S. Funk, G. Ertl, M. Bonn, Ch. Frischkorn, M. Wolf: In *Femtochemistry and Femtobiology: Ultrafast Dynamics in Molecular Science*, ed. by A. Douhal, J. Santamaria (World Scientific, Singapore 2002) p. 652
- 32 *Physik Daten*, ed. by H. Behrens, G. Ebel (Fachinformationszentrum Karlsruhe 1981)
- 33 T. Hertel, R. Fasel, G. Moos: *Appl. Phys. A* **75**, 449 (2002)
- 34 D.N. Denzler, C. Gahl, S. Wagner, R. Dudek, J. Stähler, C. Frischkorn, U. Bovensiepen, M. Wolf, G. Ertl: to be published
- 35 G. Held, D. Menzel: *Surf. Sci.* **316**, 92 (1994)
- 36 M. Wolf, A. Hotzel, E. Knoesel, D. Velic: *Phys. Rev. B* **59**, 5926 (1999)
- 37 A. Seitsonen: PhD thesis, Technische Universität Berlin (2002) [[http://edocs.tu-berlin.de/diss/2000/seitsonen\\_ari.htm](http://edocs.tu-berlin.de/diss/2000/seitsonen_ari.htm)]
- 38 M.I. Kaganov, I.M. Lifshitz, L.V. Tanatarov: *Sov. Phys. JETP* **4**, 173 (1957)
- 39 D. Palik: *Handbook of Optical Constants of Solids III* (Academic, London 1998)
- 40 Ch. Kittel: *Introduction to Solid State Physics*, 7th edn. (Wiley, New York 1996)
- 41 H. Schober, P.H. Dederichs: *Phonon States of Elements. Electron States and Fermi Surfaces of Alloys*, In *Landolt Börnstein New Ser.*, Vol. III/13a (Springer, Berlin 1981) p. 130
- 42 A.P. Cracknell: *Electron States and Fermi Surfaces of Elements*, In *Landolt Börnstein New Ser.*, Vol. III/13c (Springer, Berlin 1984) p. 315